Remote Sensing Applications: Society and Environment 39 (2025) 101656

Contents lists available at ScienceDirect

Remote Sensing Applications: Society and Environment

journal homepage: www.elsevier.com/locate/rsase

Advancing InSAR analysis: TimeSAPS for linear and nonlinear displacement modeling

Eugenia Giorgini [a,b,*], Luca Tavasci [a], Enrica Vecchi [c], Luca Poluzzi [d], Stefano Gandolfi [a]

[a] Department of Civil, Chemical, Environmental, and Materials Engineering—DICAM, University of Bologna, 40136, Bologna, Italy
[b] National Ph.D. in Earth Observation, Sapienza University of Rome, 00185, Rome, Italy
[c] Department of Civil, Environmental Engineering and Architecture-DICAAR, University of Cagliari, 09124, Cagliari, Italy
[d] University of Bologna, 40136, Bologna, Italy

ARTICLE INFO

Keywords:
Time series analysis
Persistent scatterers
Time series modeling
Ground surface movements detection
Surface motion characteristics
Nonlinear movements
Frequency analysis

ABSTRACT

The Synthetic Aperture Radar Interferometry (InSAR) technique enables precise monitoring of ground displacements over extensive areas based on radar data. While several open-source software packages have been developed for SAR data processing, most retrieve the average velocity of Persistent Scatterers (PS) clusters under the assumption of linear behavior, limiting their application in complex scenarios.

To enable more advanced and detailed analysis of InSAR time series, the TimeSAPS software package has been developed. This tool addresses the limitations of existing open-source packages, which primarily focus on linear approximations of displacement time series, by introducing advanced capabilities for analyzing both linear trends and nonlinear components. TimeSAPS performs a comprehensive analysis of PS derived from InSAR processing, characterizing time series in terms of linear trends, periodic signals, and nonlinear movements. Nonlinear components are modeled as a combination of sinusoids, each defined by its phase, amplitude, and frequency power spectrum. TimeSAPS overcomes the limitations of existing tools by providing advanced methods to recognize and model nonlinear surface movements, even when they are not known a priori.

This paper presents the theoretical foundations of TimeSAPS and demonstrates its capabilities through two case studies based on real InSAR data. These examples showcase the software's effectiveness in reconstructing nonlinear displacement patterns and identifying periodic trends. The results underline TimeSAPS's potential to analyze complex ground displacement scenarios, making it a valuable resource for the scientific and engineering communities.

1. Introduction

The Earth's surface is constantly changing as a result of natural and anthropogenic phenomena that can be classified according to their spatial scale, magnitude, risk, or rate of progression (Soldato et al., 2019; Festa et al., 2022; Mirmazloumi et al., 2022). The tools, technologies and data analysis approaches used to monitor these phenomena, have undergone considerable innovation over the years. The most widely used techniques to measure ground movements are leveling (Vanicek et al., 1980; Bitelli et al., 2000; Young, 1989), Global Navigation Satellite Systems (GNSS) (Abdalla et al., 2024; Galloway et al., 1999; Michelle et al., 2001;

* Corresponding author at: Department of Civil, Chemical, Environmental, and Materials Engineering—DICAM, University of Bologna, 40136, Bologna, Italy.
E-mail address: eugenia.giorgini@unibo.it (E. Giorgini).

https://doi.org/10.1016/j.rsase.2025.101656
Received 21 March 2025; Received in revised form 30 May 2025; Accepted 7 July 2025
Available online 17 July 2025

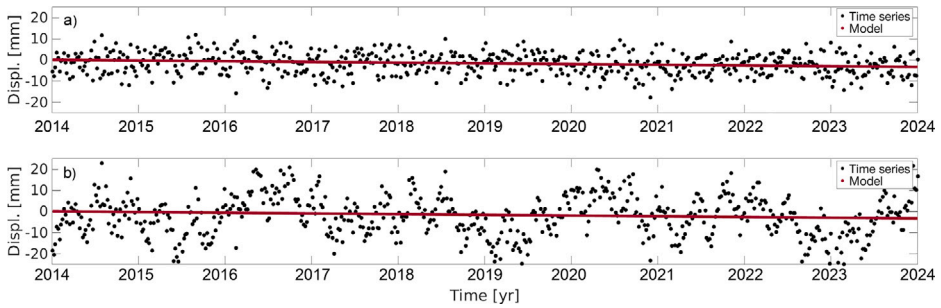

Fig. 1. Example of time series of Persistent Scatterers computed by StaMPS, mainly characterized by measurement noise and (a) a linear trend (b) nonlinear displacements. Black dots represent the InSAR displacement time series, and the red lines represented the regression straight line, not properly fitting for case (b). (For interpretation of the references to color in this figure legend, the reader is referred to the web version of this article.)

Liu et al., 2014), and, more recently, Synthetic Aperture Radar Interferometry (InSAR) (Tesauro et al., 2000; Cascini et al., 2006; Costantini et al., 2015; Ferretti et al., 2015). These three techniques allow for the study of the movements of reference elements at different spatio-temporal resolutions, as described in Bitelli et al. (2015), Brandt et al. (2020) and Giorgini et al. (2023).

The present study focuses on the InSAR technique, which offers a number of distinctive capabilities. These include the ability to acquire data over extensive areas with a high density of spatial information and reconstruct long time series (including past epochs) with year-round acquisitions, regardless of weather conditions (Hanssen, 2001; Moreira et al., 2013). During recent years, the InSAR technique has been used to monitor many movements of the Earth's surface (Massonnet and Feigl, 1998), such as subsidence (Brandt et al., 2020; Giorgini et al., 2023; Ketelaar et al., 2020; Raspini et al., 2022; Yu et al., 2013; Bitelli et al., 2025), earthquakes (Liu et al., 2004; Spaans and Hooper, 2016; Weiss et al., 2020), and landslides (Fastellini et al., 2011; Gili et al., 2000; Vecchi et al., 2024). InSAR technique exploits two or more SAR acquisitions, which are compared forming the interferogram, allowing to estimate the amplitude and the phase change of each pixel acquired over the area of interest (Hanssen, 2001). Phase variations occurring at different epochs allow to reconstruct the related time series of the displacements of the Earth's surface and to obtain their average rate of displacement variation.

Over the years, the rapid development of InSAR techniques has led to the development of several software capable of forming interferograms,ding SNAP (Foumelis et al., 2018), GAMMA (Wegmller et al., 2001) and LiCSAR (Lazecký et al., 2020). In addition, numerous algorithms for time series processing and estimation of displacement velocities have been developed (Crosetto et al., 2016). All of these algorithms compute time series from a stack of SAR images to identify pixels with stable characteristics in both time and space, called Persistent Scatterers or Distributed Scatterers. The principal algorithms are: PSInSAR (Ferretti et al., 2001), SqueeSAR (Ferretti et al., 2011), StaMPS (Hooper et al., 2004), SBAS (Berardino et al., 2002) and LiCSBAS (Morishita et al., 2020).

The selection of these stable points called "PS" carried out by these software programmes is based on the phase and amplitude characteristics of targets. For some of them, such as StaMPS, the spatial correlation between pixels is also taken into account (Hooper et al., 2004). One of the advantages of considering the spatial correlation is the capacity to detect low-amplitude targets with stable phase (Hooper et al., 2004; Hooper, 2006). For each PS, InSAR software provides a set of parameters to describe the surface displacement, including the mean velocity and the time series of displacements in the satellites' line of sight (LOS). A limitation of the InSAR available software is that they are only perform linear velocity analysis on the time series. As a result, they are unable to account for the presence of periodic signals, thus possibly affecting the accuracy of the estimated average velocity. Indeed, periodic signals contain an intrinsic trend that influences the estimate of the average velocity, which is not detectable when the motion is only linearly analyzed. This results in a less accurate estimation of the average velocity, which can be overcome by including periodic signals in the time series models.

To perform a more accurate and detailed analysis of these InSAR output time series in the frequency domain Springford et al. (2020), Vio et al. (2013) and Zechmeister and Kürster (2009), the TimeSAPS software package, Giorgini (2024) has been developed. TimeSAPS is a software tool operating on the standard output of the InSAR processing software, and enabling the characterization of linear and non-linear signals for each PS time series (Fig. 1). This is achieved through the identification of linear trends, periodic signals, and related phase and amplitude. The modeling of the PS time series allows the detection of local ground motion phenomena and the study of their spatial distribution, also enhancing performance of predictive analyses. The TimeSAPS GUI is described in Appendix A.

Over time, the analysis of InSAR time series has been applied both during the unwrapping phase, which is essential for generating the time series of Persistent Scatterers (PS) (F. et al., 2012; Osmanoğlu et al., 2016; Duan et al., 2018; Chang and Hanssen, 2016), and for modeling the generated time series to identify specific displacement characteristics (Roque et al., 2023; Hakim et al., 2024). In the latter case, various mathematical models have been explored in the literature, each tailored to specific deformation patterns and geophysical processes. Among these, notable approaches include the hyperbolic model (Park and Hong, 2021), the Kalman Filter (Dalaison and Jolivet, 2020), Deep Learning techniques (Lim and Zohren, 2021; Radman et al., 2021; Wang et al., 2023a), Monte Carlo algorithm (Wang et al., 2023b), Empirical Mode Decomposition (EMD) (Xiong et al., 2021), Convolution (Hakim et al., 2023), Fast Fourier Transformation (FFT) (Hastaoglu et al., 2023), Singular spectrum analysis (Jasir et al., 2024) and the

M-estimation method (Su et al., 2024). Several software tools have been developed and made available to the scientific community for time series analysis (Hrysiewicz et al., 2023; Pedretti et al., 2023; Roque et al., 2023); however, they differ from TimeSAPS in several key aspects. Unlike existing tools, TimeSAPS provides an advanced framework for recognizing and modeling both linear and nonlinear displacement trends, incorporating a more flexible approach to periodic signal detection and complex movement characterization. Furthermore, it offers an automated and user-friendly interface, facilitating the interpretation of InSAR-derived displacement patterns with minimal manual intervention. Additionally, TimeSAPS grants users the flexibility to search for periodic signals with user-defined frequencies, rather than relying on pre-fixed values, thus enabling a more customized investigation of deformation signals. Moreover, TimeSAPS allows for the generation of maps that visualize the nonlinear characteristics of ground movements, helping users identify previously unknown displacement patterns and gain deeper insights into surface deformation processes.

This paper aims to demonstrate the functionality and usefulness of the TimeSAPS software through the analysis of a synthetic data set and two real world scenarios. The analysis of the synthetic data set validates the software's ability to detect periodic signals within the time series and to model the time series using non-linear models. The two real case studies analyzed are located in Northern Italy, where there are various anthropogenic and natural phenomena that generate surface movements of varying magnitude. The real case studies demonstrate the usefulness of TimeSAPS in identifying non-linear ground movements, even where they are not known a priori. They also highlight the importance of detecting non-linear signals within the time series of individual PS in order to thoroughly characterize surface dynamic phenomena of different magnitudes within the real areas analyzed.

2. Materials

2.1. Synthetic datasets

To evaluate the performance of TimeSAPS in detecting periodic signals and modeling PS time series, four synthetic datasets were generated, simulating 10,000 PS under different possible scenarios. Each point was generated independently, without introducing spatial correlation within datasets. The displacement time series of each PS was modeled as a combination of different motion components, including a linear trend, periodic signals, and random noise, as described by the following equation:

$$d(t) = mt + q + \sum_{i=1}^{N} A_i sin(2\pi f_i t + \phi_i) + \epsilon(t) \quad (1)$$

where $d(t)$ represents the displacement at time t, m and q are the slope and the intercept defining the linear trend, A_i, f_i, and ϕ_i denote the amplitude, frequency, and phase of the ith periodic component, respectively, and $\epsilon(t)$ accounts for random noise. These datasets were designed to encompass a range of realistic deformation scenarios, enabling a comprehensive assessment of TimeSAPS' capabilities in identifying periodic signals and reconstructing nonlinear displacement trends. In particular two situations were considered:

1. "Known Periods" (KP) datasets: a set of displacement models built using:
   (a) random m and q
   (b) five sinusoid signals defined using:
      i. constant f for all PS: $f_1 = 0.25yr^{-1}, f_2 = 0.5yr^{-1}, f_3 = 1yr^{-1}, f_4 = 2yr^{-1}, f_5 = 4yr^{-1}$
      ii. random A and random ϕ.
   (c) one without noise $\epsilon(t) = 0$, and one with white noise $\epsilon(t)$.
2. "Unknown Frequencies" (UF) datasets: a set of displacement models built using:
   (a) random m and q
   (b) five sinusoid signals defined using:
      i. random f ($0.25yr^{-1} < f < 4yr^{-1}$), A and ϕ for each simulated PS.
   (c) one without noise $\epsilon(t) = 0$, and one with white noise $\epsilon(t)$.

To assess the impact of measurement noise on model estimation, noise components were added to both datasets. These were generated using the Matlab function "normrnd" (Marsaglia and Tsang, 1984; Trenkler, 1995), producing white noise with a Gaussian distribution characterized by a mean of $\mu = 0$ and standard deviation of $\sigma_{noise} = 10$ mm. This configuration was chosen to simulate realistic InSAR time series and to evaluate the software's performance under different signal-to-noise ratio (SNR) conditions. Additional analyses were conducted using noise levels of 1 mm and 5 mm to further assess the robustness of TimeSAPS. The results of these tests are summarized in the Appendix B but are not included in the main text to maintain readability and avoid excessive detail. All the datasets were generated over a 10-year interval with a temporal sampling of 6 days, consistent with Sentinel-1 acquisitions. Consequently, in accordance with the Nyquist limit (Austerlitz, 2003), only periodic components with durations between 3 months and 4 years were selected to ensure their detectability in the synthetic time series. Furthermore, these values were chosen to effectively represent real natural and anthropogenic ground movements, ensuring that the simulated displacements remain realistic

Table 1
Definition of the variables used for the computation of the synthetic datasets in this study. The table provides a description of each variable along with its corresponding symbol, the assigned value range and the unit of measurement.

Variable	Symbol	Interval	Unit
Slope	m	−5;0	[mm/yr]
Intercept	q	−5;5	[mm]
Amplitude 1	A_1	0;10	[mm]
Phase 1	ϕ_1	0; π	[rad]
Amplitude 2	A_2	0;8	[mm]
Phase 2	ϕ_2	π;2π	[rad]
Amplitude 3	A_3	0;6	[mm]
Phase 3	ϕ_3	2π;4π	[rad]
Amplitude 4	A_4	0;4	[mm]
Phase 4	ϕ_4	-π;0	[rad]
Amplitude 5	A_5	0;2	[mm]
Phase 5	ϕ_5	−2π; π	[rad]

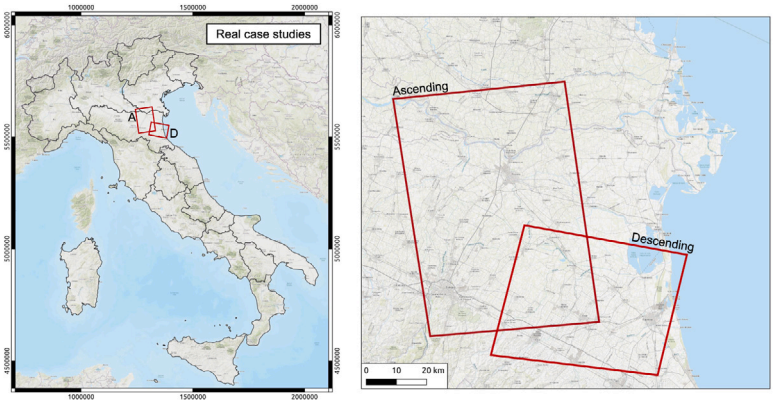

Fig. 2. Real case studies in the North of Italy, monitored using SAR Interferometry. On the left the configuration of Italy and the right an enlarged view of the specific case studies. The A indicates the Ascending frame and the D the descending one.

and do not exhibit unrealistic frequencies or amplitudes that would not typically occur in actual ground deformation processes. Similarly, amplitudes and phases were randomly assigned within predefined ranges that correspond to real-world deformation phenomena. The specific values used in the evaluation of the synthetic datasets are detailed in Table 1.

The KP dataset were designed to assess the efficacy of the implemented least-squares script in identifying the optimal values for the regression line and sinusoids parameters. Datasets UF were employed to evaluate the efficacy in detecting suitable frequencies for the construction of displacement models.

2.2. Real datasets

TimeSAPS was also tested on two real InSAR dataset measured over an area covering the eastern part of the Emilia-Romagna region (Italy), as shown in Fig. 2 (ESRI Topo World Basemap, 0000).

This area is affected by a subsidence phenomenon that has been studied for years and different natural and anthropical phenomena (Bitelli et al., 2020; Zuccarini et al., 2024). The SAR datasets were derived from seven years of observations conducted by the Sentinel-1 satellites in ascending and descending geometry, with a revisit time of 6 or 12 days for both acquisition geometries. The InSAR datasets were obtained using the SNAP-StaMPS workflow (Mancini et al., 2021) and the TRAIN tool for the purpose of applying atmospheric corrections to the data. In particular, the time series were subjected to correction using the Generic Atmospheric Correction Online Service for InSAR (GACOS) (Bekaert et al., 2015; Yu et al., 2017, 2018a,b).

3. Methods

TimeSAPS is a tool that models the time series of individual PS by identifying the regression line and eventual periodic signals, obtaining a non-linear displacement model. If we consider the time series of displacements $y(t)$, where t is the epoch of each SAR acquisition, the PS linear trend $r(t)$ can be represented using the equations:

$$r(t) = mt + q \tag{2}$$

The periodic signals are considered as the sum of sinusoids $s(t)$, each characterized by a different A, ϕ, and f:

$$s(t) = Acos(2\pi ft + \phi) \tag{3}$$

The same sinusoids can be represented using a use a trigonometric identity through two coefficients $U_1 = Acos(\phi)$ and $U_2 = -Asin(\phi)$ often taken to be normally distributed random variables (Shumway and Stoffer, 2011) as:

$$s(t) = U_1 cos(2\pi ft) + U_2 sin(2\pi ft) \tag{4}$$

Consequently, in TimeSAPS, the displacement models of each PS $l(t)$ are estimated applying the following equation, where n sinusoids are combined and v represents the residual between the original time series and the TimeSAPS model:

$$l(t) = mt + q + \sum_{i=1}^{n} [U_{1i} cos(2\pi f_i t) + U_{2i} sin(2\pi f_i t)] + v \quad i = 1, \dots, n \tag{5}$$

The amplitude and phase parameters of each sinusoid can be obtained as Shumway and Stoffer (2011):

$$A = \sqrt{U_1^2 + U_2^2} \tag{6}$$

$$\phi = tan^{-1}(-\frac{U_1}{U_2}) \quad \phi\epsilon[-\pi; \pi] \tag{7}$$

The methodology developed in TimeSAPS is designed to estimate linear and sine-wave trend parameters by minimizing the squared residuals between the input PS displacement time series and the estimated values. The inputs are the time series, the relative epochs, and the frequencies. With regard to the frequency parameter, which is an input parameter for the least-squares adjustment, two scenarios are considered. In the Known Periods case, the frequencies are defined by the user based on a priori information on the ongoing phenomenon that acts in the analyzed area. In the Unknown Frequencies case, the user selects the number of sinusoids to be used, and the relative frequencies are estimated using the Lomb–Scargle periodogram, chosen as it is capable of analyzing time series with unregular sampling, as can happen for InSAR time series (Lomb, 1976; Scargle, 1982; VanderPlas, 2018). A visual representation of the processing workflow for both scenarios is provided in Fig. 3, highlighting the differences in input requirements and frequency handling between the Known Periods (top) and Unknown Frequencies (bottom) configurations.

3.1. Known periods scenario

To provide the model parameters of the linear Eq. (5), the unweighted Gauss–Markov approach (David and Neyman, 1938) has been implemented. The algorithm allows estimating a variable number of unknown variables, dependent on the number of sinusoids to be considered and thus the number of frequencies n_f provided in input. Given the vector of the unknown x:

$$\overline{x} = [m \quad q \quad U_{1,1} \quad U_{2,1} \quad U_{1,nf} \quad U_{2,nf}] \tag{8}$$

the algorithm is set to adaptively build the design matrix B so to estimate at once all the unknown parameters in $\overline{x}$:

$for \quad n = 1, \dots, n_{epochs}$

$$B = \begin{bmatrix} t(1) - t_0 & 1 & sin(2\pi f_1 t(1)) & cos(2\pi f_1 t(1)) & \dots & sin(2\pi f_{nf} t(1)) & cos(2\pi f_{nf} t(1)) \\ \dots & 1 & \dots & \dots & \dots & \dots & \dots \\ t(n) - t_0 & 1 & sin(2\pi f_1 t(n)) & cos(2\pi f_1 t(n)) & \dots & sin(2\pi f_{nf} t(n)) & cos(2\pi f_{nf} t(n)) \end{bmatrix} \tag{9}$$

If no frequencies are available or if a linear analysis is required, the unknown considered will be m and q, consequently, the design matrix will be made of the first two columns only. The estimation of the unknown parameters is derived, as a least-squares solution from:

$$\overline{x} = (B^T B)^{-1} B^T y(t) \tag{10}$$

where B^T refers to the generalized transpose matrix.

3.2. Unknown frequencies scenario

If no-priori frequencies are known, the time series model is estimated through an iterative process, starting from the detrended input time series, $y_{det}(t)$, instead of $y(t)$. This initial $y_{det}(t)$ is determined using a linear function and serves solely to generate a detrended series for analysis with the Lomb–Scargle periodogram. The loop begins by identifying the frequency with the highest statistical power using the Lomb–Scargle periodogram, f_1, followed by estimating m_1, q_1, $U_1(1)$, $U_2(1)$ using the least squares method. A nonlinear model is then constructed, incorporating the periodic component and the newly estimated regression line. This model is subtracted from the original time series to obtain an updated detrended series. At this stage, the loop restarts and is repeated for all user-defined frequencies, iteratively refining the time series model.

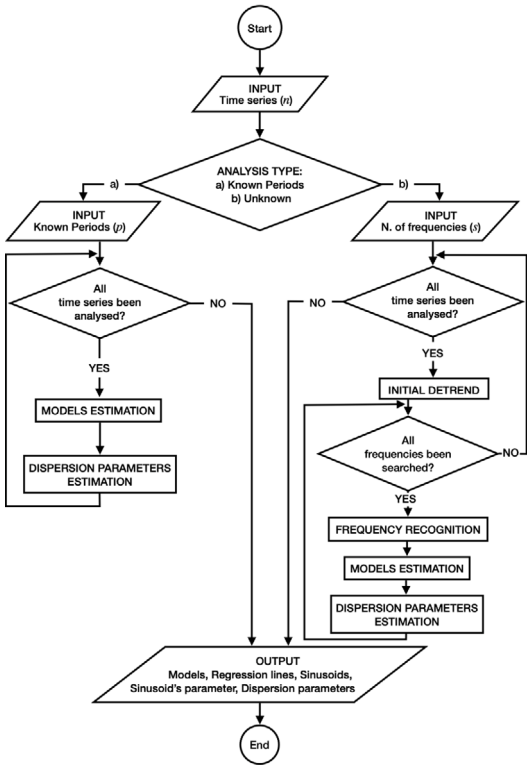

Fig. 3. Flowchart illustrating the overall TimeSAPS processing logic. The user can choose between two analysis modes: (a) Known Periods, where the periods of interest are provided a priori, and (b) Unknown Frequencies, where the number of sinusoidal components is specified and their frequencies are estimated using the Lomb–Scargle periodogram. Each time series is analyzed individually, and depending on the selected mode, appropriate steps such as detrending, frequency recognition, model estimation, and parameter extraction are applied. The process concludes with the generation of output products including the estimated models, regression lines, sinusoidal components, and dispersion parameters.

4. Results

4.1. Synthetic datasets

TimeSAPS performance was evaluated using two synthetic datasets to ascertain:

1. The efficacy of parameter estimation in modeling the time series of PS, considering the periods of the sinusoids to be utilized for modeling
2. The performance of modeling the time series of PS, given the number of sine waves to be employed.

In the initial case (KP), the periods of the sinusoids are provided as input, with the aim of evaluating the discrepancy in the estimation of the regression line parameters, specifically Δm and Δq, along with the parameters governing the generation of the sinusoids and, consequently, the non-linear model. To assess the accuracy of the non-linear model parameter estimation, the standard deviation of the residual time series between the synthetic input series and the models obtained using TimeSAPS, denoted as $\sigma_{\Delta mod}$, is calculated. In the second case (UF), the number of sinusoids used to model the time series is chosen by the user. In this scenario, the parameters Δm, Δq, and $\sigma_{\Delta mod}$, which represent the reconstruction accuracy, are provided alongside an analysis of the residuals time series.

Fig. 4: Main processing steps for displacements modeling performed in TimeSAPS. Workflow in scenario 1 is used when users already know the characteristic periods (up to 5) of the inspected signals, while workflow 2 is used to model a time series for which no a-priori insights are available.

4.1.1. Known periods scenario

The displacement time series of the KP datasets were analyzed using TimeSAPS to evaluate the accuracy of the software in estimating the unknown: m, q, $\overline{A}$, $\overline{\phi}$, where $\overline{A} = A_1, \ldots, A_n$, $\overline{\phi} = \phi_1, \ldots, \phi_n$. The exact periods used to synthesize the time series were therefore given as input. For each PS, a displacement model was then computed and compared to the synthetic models of the KP dataset. To analyze the 10,000 points composing each KP dataset, the computational burden is approximately 15 min using a 64-core Linux processor with 254 GB of RAM. The estimated and original m and q parameters were directly compared and the results in terms of statistical distribution are reported in Table 2.

Table 2
Mean and standard deviation of the residuals for the mean velocity differences (Δm) [mm/yr], intercept differences (Δq) [mm], and standard deviations ($\sigma_{\Delta mod}$) [mm] between the original time series and those estimated using TimeSAPS on the KP dataset, for the noise-free dataset and the dataset with $\sigma_{noise} = 10$ mm.

	No noise		$\sigma_{noise} = 10$ mm	
	μ	σ	μ	σ
Δm	1.70×10^{-15}	2.11×10^{-15}	−0.12	5.05×10^{-15}
Δq	6.88×10^{-3}	3.95×10^{-3}	0.72	3.95×10^{-3}
$\sigma_{\Delta mod}$	1.84×10^{-14}	7.22×10^{-15}	0.87	1.13×10^{-14}

Table 3
Residuals of the mean velocity differences (Δm) [mm/yr], intercept differences (Δq) [mm], and standard deviations ($\sigma_{\Delta mod}$) [mm] between the original time series and those estimated using TimeSAPS on the UF datasets. The time series models were created using either 5 frequencies ($\sigma_{\Delta mod}5f$) or 10 frequencies ($\sigma_{\Delta mod}10f$) for both the noise-free dataset and the dataset with $\sigma_{noise} = 10$ mm.

	No noise		$\sigma_{noise} = 10$ mm	
	μ	σ	μ	σ
Δm	1.11×10^{-2}	7.36×10^{-2}	-7.86×10^{-2}	3.86×10^{-2}
Δq	-9.59×10^{-2}	0.39	0.54	0.22
$\sigma_{\Delta mod}5f$	0.21	0.17	2.18	0.63
$\sigma_{\Delta mod}10f$	0.21	0.17	2.18	0.63

To assess the quality of the nonlinear signal reconstruction, the epoch-by-epoch residuals between the computed models and the original ones were calculated. The root-mean-square RMS of these residuals was then computed for each PS. The mean and standard deviation of the residuals RMS over the whole dataset are shown in Table 2. For all three parameters reported in Table 2, the residuals between the original and estimated values were negligible, confirming the effectiveness of the software across both synthetic datasets and under varying noise conditions.

4.1.2. Unknown frequencies scenario

The UF datasets were analyzed running TimeSAPS two times: initially searching for 5 possible sinusoids, so the same number used to create the original synthetic model, and subsequently by searching for up to 10 possible significant frequencies. To analyze the 10,000 points composing each UF dataset, the computational burden is approximately 1 h using a 64-core Linux processor with 254 GB of RAM. Table 3 report the overall statistics in the modeling errors from Δm and Δq respectively, and the $\sigma_{\Delta mod}5f$ and $\sigma_{\Delta mod}10f$ of the residuals' differences between the original series without noise and modeled time series, for the dataset with and without noise in the case of modeling the time series using at maximum 5 and 10 frequencies respectively. Errors in the m, $\sigma_{\Delta mod}5f$ and $\sigma_{\Delta mod}10f$ estimation are still below the tenth of a mm/yr, whereas the q were correctly defined within the millimeter level of accuracy. Tests on synthetic time series have shown that when the number of fundamental frequencies searched is set to match or exceed the number of frequencies used to generate the initial models, the estimated frequencies can sometimes differ significantly from the original ones. This occurs because the least squares estimation process determines the amplitudes and phases of the identified frequencies with the primary goal of minimizing residuals, rather than precisely recovering the initial frequencies. The main objective is to reconstruct the time series rather than to retrieve the exact input parameters. Notably, discrepancies in estimated frequencies were observed in cases where the original frequencies were very close to each other or when noise obscured one or more signals present in the analyzed series.

Initially, an examination of the results, reported in Table 3, for the dataset constructed in the absence of noise revealed sub-millimeter level errors. While these values are relatively small, they are not as low as those obtained when known periods are provided as input. Furthermore, the estimation errors associated with the model are significantly reduced when 10 frequencies are employed instead of the minimum number used to construct the dataset. This is likely because, when two or more sinusoids with highly similar frequency and amplitude values were used to generate the original model, the Lomb–Scargle periodogram may only identify a single frequency, corresponding to the mean of the two original frequencies. The identification of additional periodic components helps to mitigate this limitation. Additionally, this improvement is also attributable to the fact that increasing the number of model parameters enhances the fit of the data, potentially leading to (over)fitting by capturing high-frequency fluctuations caused by noise, which in turn results in a lower RMS. However, this enhancement in estimation capability by incorporating more sinusoids diminishes as σ_{noise} increases. This is expected, as peaks in the Lomb–Scargle periodogram lose statistical significance when the SNR of the time series decreases. Furthermore, both the $\sigma_{\Delta mod}5f$ and $\sigma_{\Delta mod}10f$ panels in Table 3 exhibit same behavior, as the high noise level ultimately overwhelms the signal, making it impossible to detect meaningful periodic components, regardless of the number of frequencies included in the model.

Figs. 4 and 5 illustrate the time series reconstruction capabilities of TimeSAPS, highlighting differences in the RMS of residuals between the original series and the models obtained with TimeSAPS when searching for 10 frequencies. These comparisons are made for both the noise-free dataset (Fig. 4) and the dataset with $\sigma_{noise} = 10$ mm (Fig. 5). A detailed analysis of the cases with the lowest standard deviations in Fig. 4 shows that, in the absence of noise that could hinder signal detection, the TimeSAPS algorithm can reconstruct the time series pattern with a standard deviation of less than one millimeter. The residual time series shown in Fig. 4 correspond to signals whose amplitudes and associated frequencies render them statistically insignificant in the Lomb–Scargle

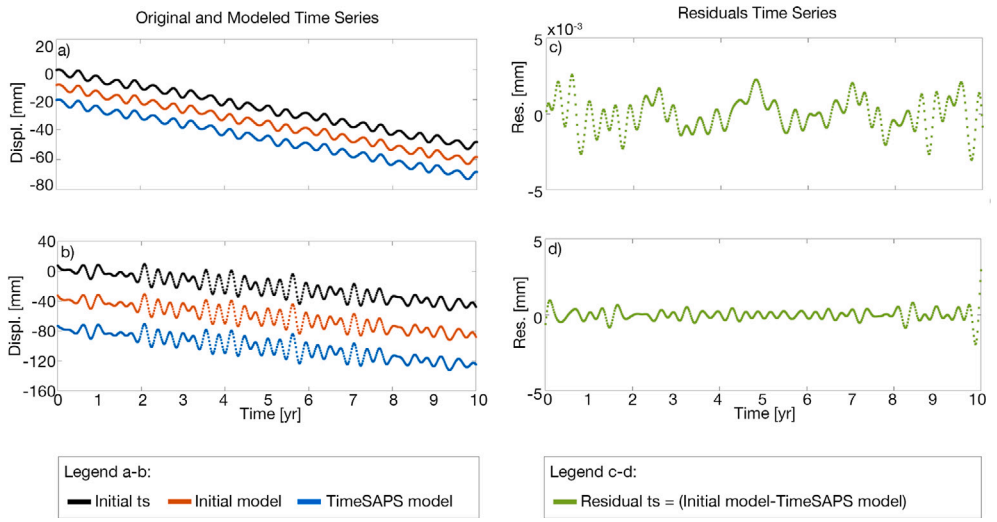

Fig. 4. Example of nonlinear model reconstruction from UF datasets time series without noise. The right plots display the residual time series, whereas the left plots show the original time series (black dots), the reference signals (red lines), and the computed TimeSAPS models (blue lines). A bias of −10 mm was applied to the initial models, while a bias of −20 mm was applied to the TimeSAPS models for better visualization. Panel (a) show cases with the lowest $\sigma_{\Delta mod}$, while (b) represent the one with the highest $\sigma_{\Delta mod}$. (For interpretation of the references to color in this figure legend, the reader is referred to the web version of this article.)

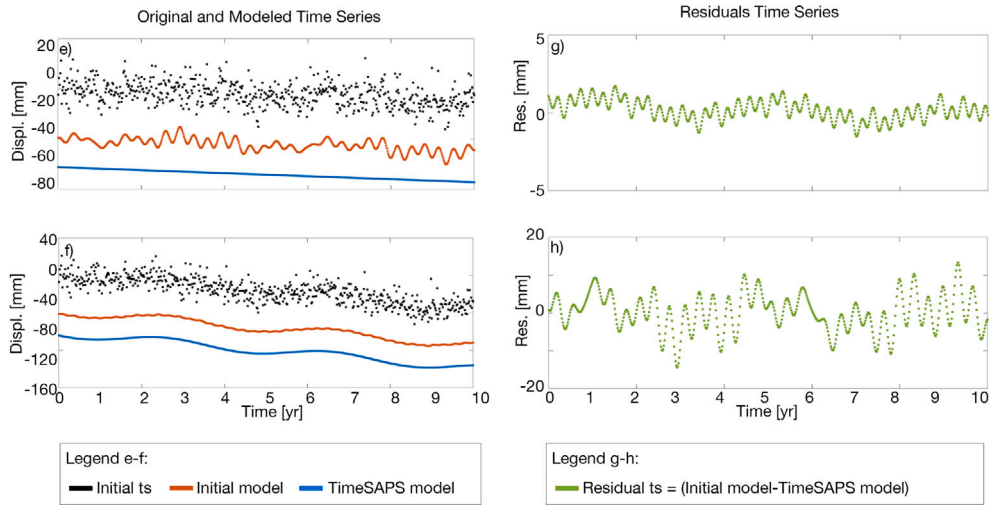

Fig. 5. Example of nonlinear model reconstruction from UF datasets time series without σ_{noise} = 10 mm. The right plots display the residual time series, whereas the left plots show the original time series (black dots), the reference signals (red lines), and the computed TimeSAPS models (blue lines). A bias of −40 mm was applied to the initial models, while a bias of −80 mm was applied to the TimeSAPS models for better visualization. Panel (e) show cases with the lowest $\sigma_{\Delta mod}$, while (f) represent the one with the highest $\sigma_{\Delta mod}$. (For interpretation of the references to color in this figure legend, the reader is referred to the web version of this article.)

periodogram, particularly when compared to the dominant signals in the series. Conversely, in Fig. 5, the residual time series result from the inability to identify one or more periodic signals within the series (Fig. 5, case e) or from the complete absence of signal recognition due to overwhelming noise (Fig. 5, case f). In the latter scenario, TimeSAPS reconstructs only the regression line of the time series.

4.2. Real case studies

Following the evaluation of TimeSAPS's time series analysis capabilities on synthetic datasets, two real-world areas monitored by Sentinel-1 satellite data were selected for further analysis. The SAR acquisitions were processed using the SNAP-StaMPS workflow to identify persistent scatterers and generate the corresponding time series. The resulting InSAR datasets were then analyzed with TimeSAPS. Initially, the mean velocity of the PS was retrieved. In the ascending frame, the Known Periods algorithm was applied to

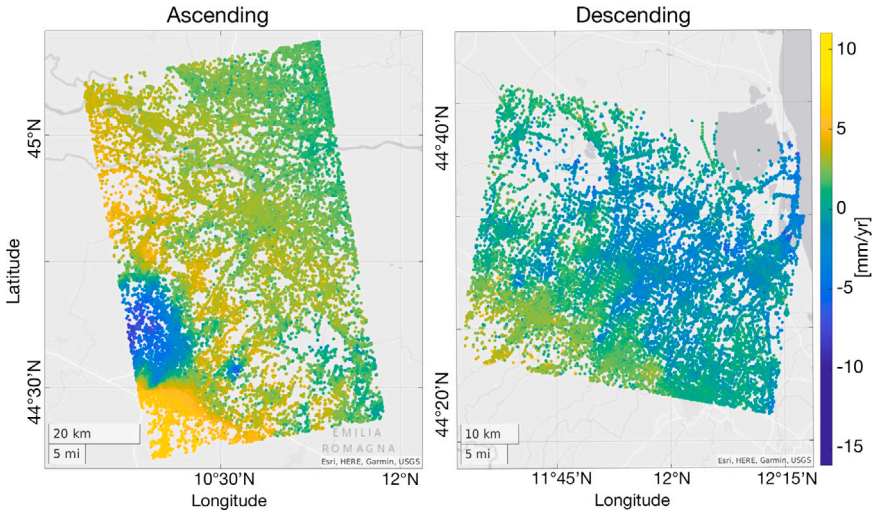

Fig. 6. Mean velocity of the PS in the ascending (left) and the descending (right) frame chose as case studies expressed in mm/yr. (For interpretation of the references to color in this figure legend, the reader is referred to the web version of this article.)

detect periodic movements at predefined periods. In the descending frame, the Unknown Frequency algorithm was used to model the PS time series with a chosen number of sinusoids, enabling the recognition and representation of possible nonlinear displacements within the area of interest.

4.2.1. Linear displacement model

One of the earliest products that TimeSAPS can return is the average velocity, estimated by assuming a linear model of PS displacement. As showed in Figure, the average velocities of ascending PS (left) and descending PS (right) obtained on the areas reported in Fig. 2 are presented.

As illustrated in Fig. 6, the well-known phenomenon of subsidence can be observed in the area surrounding Bologna in the ascending frame (blue dots). In the descending frame, a subsidence phenomenon that is more attenuated but still present and characteristic of the monitored area can be observed (light blue dots). With regard to the presence of possible non-linear phenomena, it is not yet possible to deduce anything from the linear speed of the PS. It is crucial to emphasize that these values do not consider the presence of periodic signals, characterized by an intrinsic trend, when present within the time series. When TimeSAPS is utilized in conjunction with the Known Periods or the Unknown Frequency analyses, the estimated average velocities are returned, having been stripped of the potential influences of periodic signals.

4.2.2. Known periods analysis

The analysis of known periods aids in identifying periodic movements characterized by specific durations. Considering the typical periods associated with natural and anthropogenic phenomena that induce surface movements, the periods investigated in the PS time series of case study A (Fig. 2) are: 1 year, 6 months, 2 years, and 4 years. The Known Periods analysis leads to the creation of maps representing the spatial distribution of the amplitude of both the final model and the single sinusoids that compose the model of the PS time series. Fig. 7 shows, both the total amplitude of the PS patterns and each of the amplitudes associated with the individual periods obtained in the area of interest.

As demonstrated in Fig. 7, the application of four sinusoids for modeling the time series results in the identification of regions characterized by elevated total signal amplitude values. The extent of these regions varies according to the phenomena generating these oscillatory ground motions. For instance, area A delineates the amplitudes of ground displacements in the area above a gas storage facility. In contrast, areas B, C and D are attributed to local anthropogenic activities. Furthermore, when looking at the signal amplitudes associated with each frequency, it can be observed that the highest amplitudes are only associated with the annual periodic signals. The semi-annual, bi-annual and quadrennial components then helped to identify the high amplitude regions indicated by the arrows in Fig. 7. The PS indicated by the arrows are those with the largest amplitudes. The relative time series are shown in Fig. 8, which shows that the models are composed of sinusoids having the same periods (the one imposed to carry out the analysis) but with different associated amplitudes. The different amplitudes are estimated in order to represent with the greatest accuracy, in the least squares sense, the series of PS to be analyzed.

4.2.3. Unknown frequencies analysis

The InSAR dataset was analyzed using the TimeSAPS tool, with the Unknown Frequency algorithm with $n_f = 4$ employed to model the time series of the PS with a maximum of 4 frequencies. This approach was adopted in order to provide a more detailed description of any potential non-linear movements.

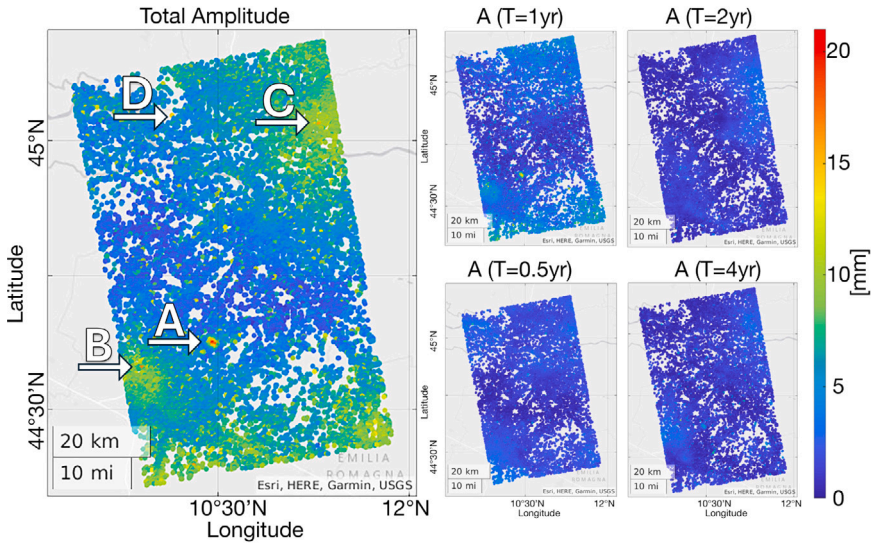

Fig. 7. Maps of the obtained Amplitudes. On the left the overall amplitude of the TimeSAPS obtained model, on the right the single amplitudes associated to the fixed periods: on the top $1yr$ (left), $2yr$ (right), on the bottom $0.5yr$ (left), $4yr$ (right).

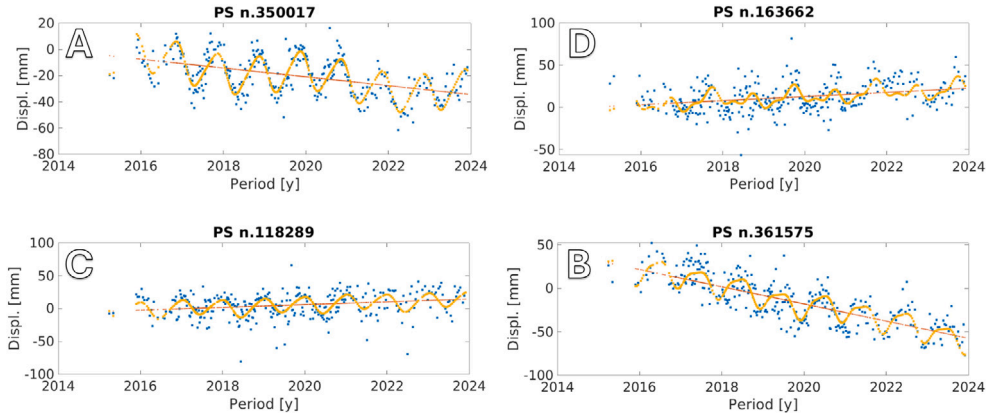

Fig. 8. Comparison between StaMPS model (red dots) and TimeSAPS model (yellow dots) computed from the time series (blue dots) of the PS spotted in Fig. 7 performing a Known Periods Analysis. (For interpretation of the references to color in this figure legend, the reader is referred to the web version of this article.)

Fig. 9 illustrates the discrepancies between the StaMPS and the TimeSAPS standard deviation of the differences between the original time series and a model evaluated under the linear hypothesis (StaMPS) and the model evaluated under the non-linear hypothesis (TimeSAPS). Furthermore, Fig. 10 demonstrates that models derived under the linear hypothesis exhibit a significantly elevated standard deviation of residuals in comparison to those generated by TimeSAPS in specific areas where some seasonal and non-linear phenomena are occurring. By analyzing the standard deviation differences, it is possible to identify distinct clusters of PS exhibiting a significantly elevated value in comparison to the surrounding area. The elevated standard deviation values suggest that the model generated with TimeSAPS exhibits a lesser degree of divergence from the original PS time series in comparison to the model derived with StaMPS. Fig. 10 illustrates the four time series with the highest standard deviation difference values, characterized by different nonlinear phenomena.

The time series illustrated in Fig. 10 describe phenomena that have yet to be identified. To conduct a comprehensive analysis of time series E (Fig. 10) and ascertain significant insights into the patterns observed in this region, the study area was restricted to the latitude range of 44° 22′N to 44° 26′N and the longitude range of 11° 39′E to 11° 41′E. Fig. 11 provide an overview of the amplitudes of the sinusoids related to the three frequencies identified for each PS. Fig. 11a illustrates how the most powerful sinusoid signals have predominantly annual periods and are related to the bigger amplitudes. Other sinusoids characterized by significant amplitudes are depicted in Fig. 11b and exhibit periods ranging from six months to over two years, which combines their effects to the yearly signals previously defined. Those sinusoids of point A associated to the third frequency (Fig. 11c) have negligible amplitudes over the analyzed region. The analysis in Fig. 11 demonstrates that TimeSAPS enables the identification and modeling

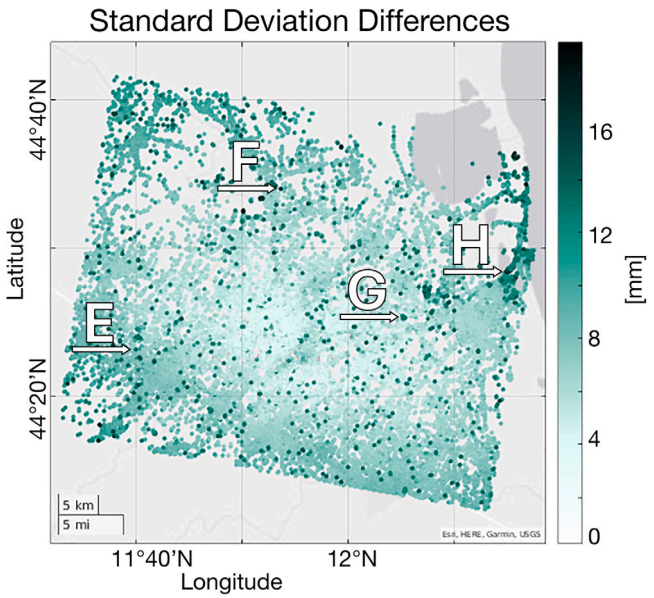

Fig. 9. Standard deviation difference map calculated with StaMPS (straight line models) and TimeSAPS (nonlinear models computed considering 4 unknown frequencies). The letters and the arrow highlight four of the PS showing the higher impact of using TimeSAPS for signal reconstruction, which details are reported in Fig. 10.

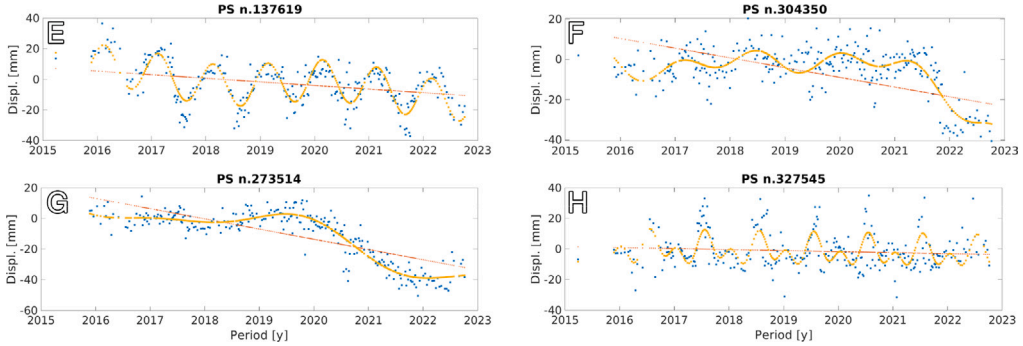

Fig. 10. Comparison between StaMPS model (red dots) and TimeSAPS model (yellow dots) computed from the time series (blue dots) of the PS spotted in Fig. 9 performing an Unknown Frequencies Analysis. (For interpretation of the references to color in this figure legend, the reader is referred to the web version of this article.)

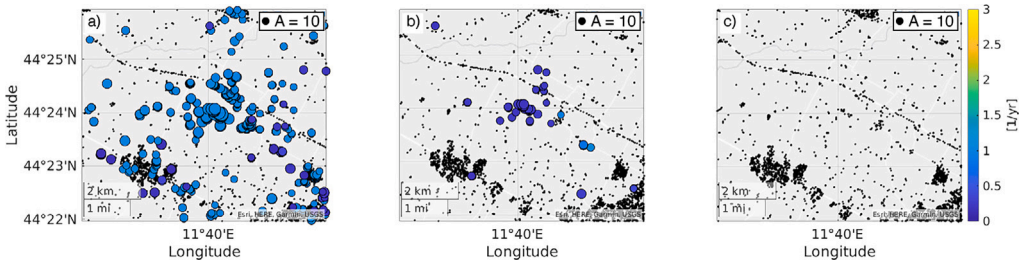

Fig. 11. For each PS in the case study area, frequencies values (circle colors) and related amplitudes (circle dimension) are shown for the first (a), second (b) and third (c) sinusoids estimated using Time SAPS. (For interpretation of the references to color in this figure legend, the reader is referred to the web version of this article.)

of specific ground motion phenomena by effectively capturing both the linear and nonlinear components of Persistent Scatterers time series.

5. Discussson

This work introduced and evaluated TimeSAPS, a novel software package for the decomposition and reconstruction of InSAR time series, capable of modeling both linear trends and multiple nonlinear periodic components. Two processing workflows were developed depending on the availability of prior information on periodicities: the ‘‘Known Periods’’ and ‘‘Unknown Frequencies’’ approaches. TimeSAPS demonstrated high accuracy in both synthetic and real datasets, effectively capturing complex displacement dynamics.

TimeSAPS can be conceptually compared to popular time series decomposition methods such as Independent Component Analysis (ICA), Hyvärinen et al. (2001), Singular Spectrum Analysis (SSA), (Elsner and Tsonis, 1996), and Empirical Mode Decomposition (EMD), (Zeiler et al., 2010). Each of these techniques offers unique advantages:

- ICA is effective in separating statistically independent components, often useful in noise reduction and blind source separation. However, its performance strongly depends on the statistical assumptions and can struggle when sources are not truly independent or when components are temporally correlated.
- SSA decomposes time series into trend, oscillatory components, and noise, offering good interpretability. Yet, it requires careful selection of the window length and often lacks a direct link to physical frequencies, limiting its utility for geophysical time series with known or expected periodicities.
- EMD, being fully data-driven, is effective for nonlinear and nonstationary signals. However, it can suffer from mode mixing, lacks robustness to noise, and does not guarantee physically meaningful decomposition components.

In contrast, TimeSAPS combines a parametric approach with physical interpretability: the decomposition is directly linked to user-defined or data-driven frequencies, and results are expressed in terms of meaningful parameters (amplitudes, phases, frequencies, regression coefficients). This makes TimeSAPS particularly suitable for applications where periodic processes (e.g., seasonal deformation, cyclic loading) are expected and interpretable.

The computational cost of TimeSAPS is moderate and scales linearly with the number of Persistent Scatterers (PS) and candidate frequencies. For the Known Periods (KP) dataset consisting of 10,000 points, the complete reconstruction process—including regression, sinusoidal fitting, and parameter extraction—takes approximately 15 min on a 64-core Linux workstation with 254 GB of RAM. In the case of the Unknown Frequencies (UF) dataset, analyzing 10,000 points while searching for five sinusoids requires about 1 h under the same hardware conditions. Although this performance is suitable for offline processing—particularly considering the interpretability of the resulting models—future optimizations may be needed to reduce runtime for larger datasets or near-real-time applications. In terms of usability, TimeSAPS is fully scriptable, supports batch processing, and is compatible with standard InSAR outputs, making it easy to integrate into existing processing pipelines.

One of the main strengths of TimeSAPS lies in its ability to separately estimate both the linear and periodic components of ground displacement, under both user-guided and data-driven configurations. It has shown to perform well even in noisy conditions, particularly when signal amplitudes are sufficiently strong. However, TimeSAPS also has limitations. In the presence of high noise levels or weak signals, the Lomb–Scargle-based frequency recognition may fail to isolate significant components, leading to partial or oversimplified reconstructions. Moreover, the assumption of sinusoidal components may not fully capture abrupt or transient behaviors, limiting the applicability of the method in certain contexts such as coseismic or volcanic deformation with nonlinear onset.

Future developments may include the integration of advanced spectral selection methods, adaptive frequency scanning, or hybrid techniques combining TimeSAPS with SSA or machine learning-based signal classification. Additionally, extending the method to work with multidimensional or spatially correlated time series could further enhance its utility for large-scale geodetic monitoring.

6. Conclusion

This work has presented TimeSAPS, a novel software tool for the analysis of InSAR-derived Persistent Scatterer time series, designed to accurately model both linear and nonlinear displacement trends. Two complementary approaches were implemented: one based on user-defined periodicities, and another enabling data-driven frequency identification using the Lomb–Scargle periodogram.

Through tests on both synthetic and real datasets, TimeSAPS proved effective in identifying and reconstructing complex displacement signals, even under low signal-to-noise conditions. The software extends the capabilities of conventional tools by offering a flexible, interpretable, and user-friendly framework for periodic signal modeling.

The graphical interface and broad compatibility with time series data make TimeSAPS a practical solution for researchers and practitioners in geohazard monitoring, infrastructure assessment, and environmental analysis.

Looking ahead, TimeSAPS will evolve by integrating advanced signal decomposition techniques and machine learning-based classification, further enhancing its ability to detect and interpret complex deformation patterns.

In summary, TimeSAPS represents a valuable advancement for InSAR time series modeling, bridging the gap between linear assumptions and the complex realities of ground motion analysis.

CRediT authorship contribution statement

Eugenia Giorgini: Conceptualization, Writing – review & editing, Investigation, Writing – original draft, Software, Methodology, Formal analysis, Visualization, Validation, Resources, Data curation. **Luca Tavasci:** Conceptualization, Methodology, Validation, Formal analysis. **Enrica Vecchi:** Writing – review & editing. **Luca Poluzzi:** Conceptualization, Software, Formal analysis, Methodology. **Stefano Gandolfi:** Writing – review & editing, Supervision, Project administration, Conceptualization, Resources, Formal analysis, Visualization, Funding acquisition.

Declaration of competing interest

The authors declare that they have no known competing financial interests or personal relationships that could have appeared to influence the work reported in this paper.

Acknowledgment

Funded by the European Union - PNRR351 RICERCA, Mission 4, Component 1, CUP351: B53C22004370006

Appendix A. TimeSAPS GUI

The layout of TimeSAPS GUI version is structured in four main sections that comprise the left-hand panel. The right-hand tabs are designed for displaying the obtained results, as shown in Fig. A.12.

More in detail, in the left panel, the first and last sections are responsible for handling input and output data, respectively. The middle sections are dedicated to the customization of the time series analysis. In the "Load Data" section the user can specify the folder containing the time series to be analyzed and saved in the "StaMPS format". In this section, the user can also crop the area of interest to reduce the computational burden. The bottom section, "Export Data", enables the user to save the estimated data in three distinct formats: .shp, .mat, and .csv. The outputs of TimeSAPS comprise the models of the time series of PS, along with the parameters that generate these models (m, q, A, ϕ, and f). The middle steps allow performing the time series analysis for two different scenarios:

1. "Known Periods": this section allows to input the frequencies values to estimate up to five sinusoids to be combined.
2. "Unknown Frequencies": this section enables the detection of the n_f, most powerful frequencies within the PS time series using the Lomb–Scargle periodogram, returning the coefficients of the related sinusoids.

The right panel (Fig. A.13) displays the input data and the obtained results. It consists of 5 sections:

1. "Loaded Data": displays the loaded PS, showing the average speed in mm/yr.
2. "Known Periods": displays the values obtained for each PS after the completion of a Known Periods analysis.
3. "KP – PS Comparison": displays the original time series and the estimated model of a PS of interest together with its estimated parameters.
4. "Unknown Frequencies": displays the values obtained for each PS after the completion of a Unknow Frequencies analysis.
5. "UF – PS Comparison": displays the original time series and the estimated model of a PS of interest together with its estimated parameters and the Lomb–Scargle Periodogram.

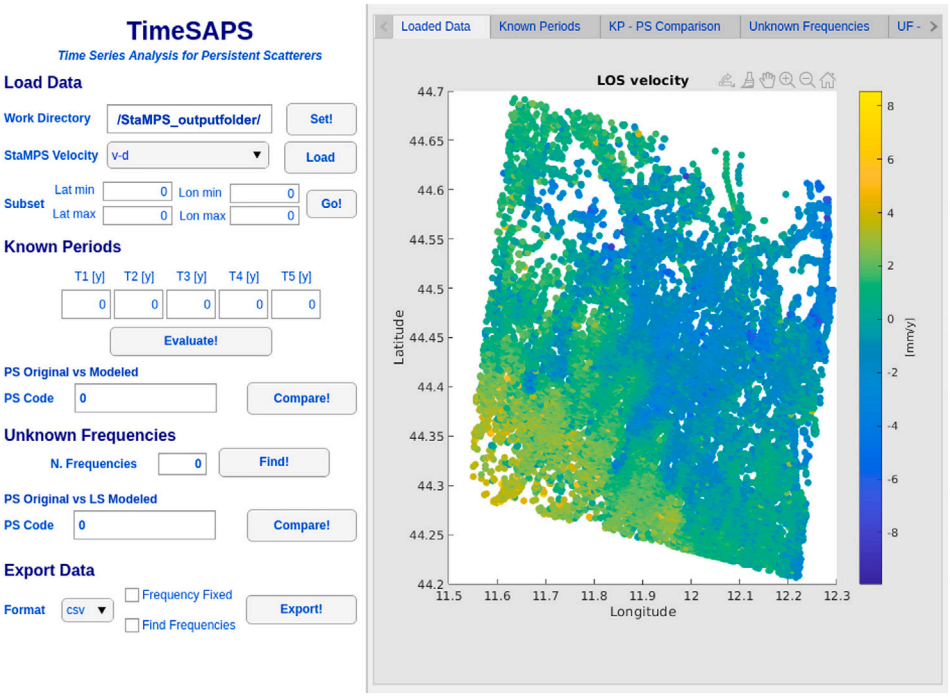

Fig. A.12. TimeSAPS' main window: the menu on the left panel allows setting the analysis parameters, while the right panel is dedicated to show the results.

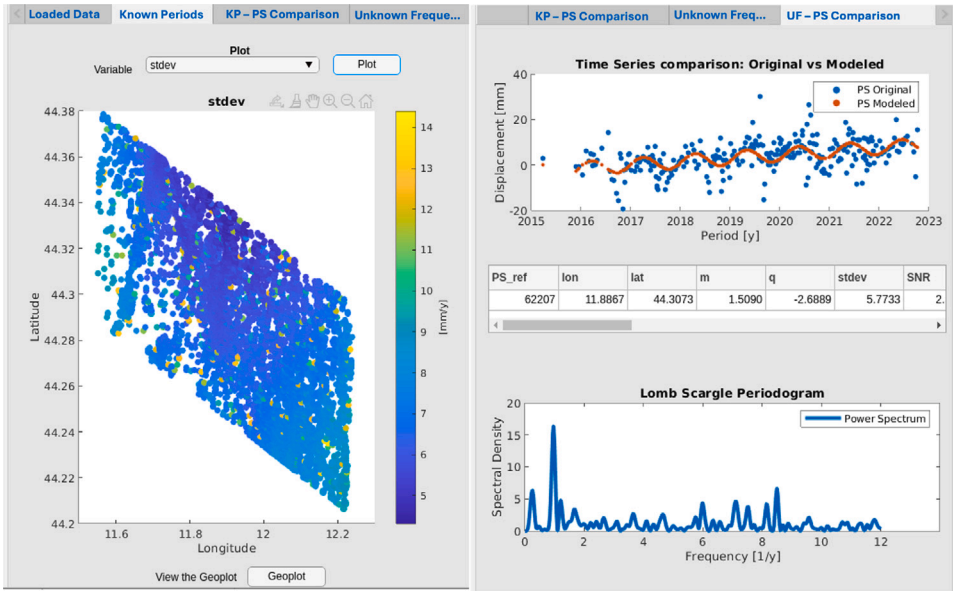

Fig. A.13. Example of TimeSAPS's output displayed in the right panel. On the left the "Known Periods" tab where standard deviations of each PS residuals to the nonlinear model are shown. On the right, an example of a PS details tab related to an "Unknown Frequency" processing: the time series, the nonlinear model, the related Lomb–Scargle periodogram and numerical parameters of the inspected PS are shown.

Table B.4
Mean and standard deviation of the residuals for the mean velocity differences (Δm) [mm/yr], intercept differences (Δq) [mm], and standard deviations ($\sigma_{\Delta mod}$) [mm] between the original time series and those estimated using TimeSAPS on the KP dataset, for the dataset with $\sigma_{noise} = 1$ mm and the dataset with $\sigma_{noise} = 5$ mm.

	$\sigma_{noise} = 1$ mm		$\sigma_{noise} = 5$ mm	
	μ	σ	μ	σ
Δm	-3.89×10^{-3}	2.11×10^{-15}	-6.26×10^{-2}	2.65×10^{-15}
Δq	-3.56×10^{-2}	3.94×10^{-3}	8.07×10^{-2}	3.94×10^{-3}
$\sigma_{\Delta mod}$	0.12	4.32×10^{-15}	0.78	3.70×10^{-14}

Table B.5
Residuals of the mean velocity differences (Δm) [mm/yr], intercept differences (Δq) [mm], and standard deviations ($\sigma_{\Delta mod}$) [mm] between the original time series and those estimated using TimeSAPS on the UF datasets. The time series models were created using either 5 frequencies ($\sigma_{\Delta mod} 5f$) or 10 frequencies ($\sigma_{\Delta mod} 10f$) for both the dataset with $\sigma_{noise} = 1$ mm and the dataset with $\sigma_{noise} = 5$ mm.

	$\sigma_{noise} = 1$ mm		$\sigma_{noise} = 5$ mm	
	μ	σ	μ	σ
Δm	3.55×10^{-2}	7.36×10^{-2}	6.61×10^{-2}	2.45×10^{-2}
Δq	−0.24	0.39	−0.53	0.14
$\sigma_{\Delta mod} 5f$	0.21	0.17	1.11	0.31
$\sigma_{\Delta mod} 10f$	0.21	0.17	1.11	0.31

Appendix B. Additional analysis of TimeSAPS performance with different noise levels

To further evaluate the capabilities of TimeSAPS, we conducted additional analyses using four synthetic datasets derived by adding different noise levels to the KP and UF datasets. Specifically, a Gaussian noise with a standard deviation of 1 mm was applied to both KP and UF datasets, and a Gaussian noise with a standard deviation of 5 mm was applied to the same datasets.

The results for the KP datasets are presented in Table B.4, which illustrates the differences in the estimated parameters m and q compared to their initial values. Additionally, the standard deviation of the residuals, computed as the difference between the initial time series and the corresponding series modeled with TimeSAPS, is also reported.

For the UF datasets, Table B.5 reports the differences in the estimated parameters m and q relative to their initial values. Moreover, the standard deviation of the residuals is reported for both cases where TimeSAPS was used with 5 frequencies and 10 frequencies to model the time series.

These additional results provide further insights into the robustness of TimeSAPS under different noise conditions and highlight its capability to effectively model displacement time series while accounting for increasing levels of noise.

Both tables confirm the observations discussed in the Results section of the article: as the noise level increases, the differences between the initial parameters and those estimated by TimeSAPS also increase, albeit to a limited extent.

Data availability

Data will be made available on request.

References

Abdalla, A., Fernandes, R., Bos, M., Fadil, A., 2024. Land Subsidence Monitoring and Analysis in Louisiana Using GNSS Daily Solutions. Springer Nature, pp. 21–24. http://dx.doi.org/10.1007/978-3-031-43807-3_4, chapter Advances in Science, Technology and Innovation.

Austerlitz, H., 2003. Analog/Digital Conversions. Elsevier, pp. 51–77. http://dx.doi.org/10.1016/B978-012068377-2/50004-8, chapter 4.

Bekaert, D., Walters, R., Wright, T., Hooper, A., Parker, D., 2015. Statistical comparison of InSAR tropospheric correction techniques. Remote Sens. Environ. 170, 40–47. http://dx.doi.org/10.1016/j.rse.2015.08.035.

Berardino, P., Fornaro, G., Lanari, R., Sansosti, E., 2002. A new algorithm for surface deformation monitoring based on small baseline differential SAR interferograms. IEEE Trans. Geosci. Remote Sens. 40 (11), 2375–2383. http://dx.doi.org/10.1109/TGRS.2002.803792.

Bitelli, G., Bonsignore, F., Conte, S.D., Franci, F., Lambertini, A., Novali, F., Severi, P., Vittuari, L., 2020. Updating the subsidence map of Emilia-Romagna region (Italy) by integration of SAR interferometry and GNSS time series: the 2011–2016 period. Proc. Int. Assoc. Hydrol. Sci. 382, 39–44. http://dx.doi.org/10.5194/piahs-382-39-2020.

Bitelli, G., Bonsignore, F., Pellegrino, I., Vittuari, L., 2015. Evolution of the techniques for subsidence monitoring at regional scale: the case of Emilia-Romagna region (Italy). Proc. Int. Assoc. Hydrol. Sci. 372, 315–321. http://dx.doi.org/10.5194/piahs-372-315-2015.

Bitelli, G., Bonsignore, F., Unguendoli, M., 2000. Levelling and GPS networks to monitor ground subsidence in the southern po valley. J. Geodyn. 30, 355–369. http://dx.doi.org/10.1016/S0264-3707(99)00071-X.

Bitelli, G., Ferretti, A., Giannico, C., Giorgini, E., Lambertini, A., Marcaccio, M., Mazzei, M., Vittuari, L., 2025. Subsidence monitoring in emilia-romagna region (Italy) from 2016 to 2021: From InSAR and GNSS integration to data analysis. Remote. Sens. 17 (6), http://dx.doi.org/10.3390/rs17060947, URL: https://www.mdpi.com/2072-4292/17/6/947.

Brandt, J.T., Sneed, M., Danskin, W.R., 2020. Detection and measurement of land subsidence and uplift using interferometric synthetic aperture radar, San Diego, California, USA, 2016–2018. Proc. Int. Assoc. Hydrol. Sci. 382, 45–49. http://dx.doi.org/10.5194/piahs-382-45-2020.

Cascini, L., Ferlisi, S., Fornaro, G., Lanari, R., Peduto, D., Zeni, G., 2006. Subsidence monitoring in sarno urban area via multi-temporal DInSAR technique. Int. J. Remote Sens. 27, 1709–1716. http://dx.doi.org/10.1080/01431160500296024.

Chang, L., Hanssen, R.F., 2016. A probabilistic approach for InSAR time-series postprocessing. IEEE Trans. Geosci. Remote Sens. 54, 421–430. http://dx.doi.org/10.1109/TGRS.2015.2459037.

Costantini, M., Minati, F., Ciminelli, M.G., Ferretti, A., Costabile, S., 2015. Nationwide ground deformation monitoring by persistent scatterer interferometry. In: 2015 IEEE International Geoscience and Remote Sensing Symposium. IGARSS, pp. 1472–1475. http://dx.doi.org/10.1109/IGARSS.2015.7326057.

Crosetto, M., Monserrat, O., Cuevas-González, M., Devanthéry, N., Crippa, B., 2016. Persistent scatterer interferometry: A review. ISPRS J. Photogramm. Remote Sens. 115, 78–89. http://dx.doi.org/10.1016/j.isprsjprs.2015.10.011.

Dalaison, M., Jolivet, R., 2020. A Kalman filter time series analysis method for InSAR. J. Geophys. Res.: Solid Earth 125, http://dx.doi.org/10.1029/2019JB019150.

David, F.N., Neyman, J., 1938. Extension of the Markoff Theorem on Least Squares. London University College, Department of Statistics.

Duan, W., Zhang, H., Wang, C., 2018. Deformation estimation for time series InSAR using simulated annealing algorithm. Sensors 19, 115. http://dx.doi.org/10.3390/s19010115.

Elsner, J.B., Tsonis, A.A., 1996. Singular Spectrum Analysis. Springer US, Boston, MA, http://dx.doi.org/10.1007/978-1-4757-2514-8.

ESRI Topo World Basemap, URL: https://services.arcgisonline.com/ArcGIS/rest/services/NatGeo_World_Map/MapServer.

F., H.R., S., S.-E., A., H., F., V.L., Liu, J., 2012. Separating non-linear deformation and atmospheric phase screen (APS) for INSAR time series analysis using least-square collocation. In: SP-697, E. (Ed.), Proceedings of Fringe 2011, Held 19-23 September, 2011 in Frascati, Italy. pp. 1–5.

Fastellini, G., Radicioni, F., Stoppini, A., 2011. The assisi landslide monitoring: a multi-year activity based on geomatic techniques. Appl. Geomat. 3, 91–100. http://dx.doi.org/10.1007/s12518-010-0042-9.

Ferretti, A., Colombo, D., Fumagalli, A., Novali, F., Rucci, A., 2015. InSAR data for monitoring land subsidence: time to think big. Proc. Int. Assoc. Hydrol. Sci. 372, 331–334. http://dx.doi.org/10.5194/piahs-372-331-2015.

Ferretti, A., Fumagalli, A., Novali, F., Prati, C., Rocca, F., Rucci, A., 2011. A new algorithm for processing interferometric data-stacks: SqueeSAR. IEEE Trans. Geosci. Remote Sens. 49, 3460–3470. http://dx.doi.org/10.1109/TGRS.2011.2124465.

Ferretti, A., Prati, C., Rocca, F., 2001. Permanent scatterers in SAR interferometry. IEEE Trans. Geosci. Remote Sens. 39, 8–20. http://dx.doi.org/10.1109/36.898661.

Festa, D., Bonano, M., Casagli, N., Confuorto, P., Luca, C.D., Soldato, M.D., Lanari, R., Lu, P., Manunta, M., Manzo, M., Onorato, G., Raspini, F., Zinno, I., Casu, F., 2022. Nation-wide mapping and classification of ground deformation phenomena through the spatial clustering of P-SBAS InSAR measurements: Italy case study. ISPRS J. Photogramm. Remote Sens. 189, 1–22. http://dx.doi.org/10.1016/j.isprsjprs.2022.04.022.

Foumelis, M., Delgado Blasco, J.M., Desnos, Y.-L., Engdahl, M., Fernandez, D., Veci, L., Lu, J., Wong, C., 2018. Esa snap - stamps integrated processing for sentinel-1 persistent scatterer interferometry. In: IGARSS 2018 - 2018 IEEE International Geoscience and Remote Sensing Symposium. pp. 1364–1367. http://dx.doi.org/10.1109/IGARSS.2018.8519545.

Galloway, D., Jones, D.R., Ingebritsen, S., 1999. Land subsidence in the United States. U. S. Geol. Surv. Circ. USGS Circ. 1182.

Gili, J.A., Corominas, J., Rius, J., 2000. Using global positioning system techniques in landslide monitoring. Eng. Geol. 55, 167–192. http://dx.doi.org/10.1016/S0013-7952(99)00127-1.

Giorgini, E., 2024. TimeSAPS v.1.0, 2024. http://dx.doi.org/10.5281/zenodo.13867407.

Giorgini, E., Orellana, F., Arratia, C., Tavasci, L., Montalva, G., Moreno, M., Gandolfi, S., 2023. InSAR monitoring using persistent scatterer interferometry (PSI) and small baseline subset (SBAS) techniques for ground deformation measurement in Metropolitan Area of Concepción, Chile. Remote. Sens. 15, 5700. http://dx.doi.org/10.3390/rs15245700.

Hakim, W.L., Fadhillah, M.F., Lee, S., Park, S., Baek, W.-K., Hong, C.-K., Kim, H.-C., Lee, C.-W., 2024. Time-series InSAR measurement using ICOPS and estimation of along-track surface deformation using MAI during the 2021 eruption of Fagradalsfjall Volcano, Iceland. Sci. Rep. 14, 30709. http://dx.doi.org/10.1038/s41598-024-79128-1.

Hakim, W.L., Fadhillah, M.F., Park, S., Pradhan, B., Won, J.-S., Lee, C.-W., 2023. Insar time-series analysis and susceptibility mapping for land subsidence in Semarang, Indonesia using convolutional neural network and support vector regression. Remote Sens. Environ. 287, 113453. http://dx.doi.org/10.1016/j.rse.2023.113453.

Hanssen, R.F., 2001. Radar Interferometry. Vol. 2, Springer Netherlands, Dordrecht, http://dx.doi.org/10.1007/0-306-47633-9.

Hastaoglu, K.O., Poyraz, F., Erdogan, H., Tiryakioglu, I., Ozkaymak, C., Duman, H., Gül, Y., Guler, S., Dogan, A., Gul, Y., 2023. Determination of periodic deformation from InSAR results using the FFT time series analysis method in Gediz Graben. Nat. Hazards 117, 491–517. http://dx.doi.org/10.1007/s11069-023-05870-w.

Hooper, A., 2006. Persistent scatter radar interferometry for crustal deformation studies and modeling of volcanic deformation. J. Gepophys. Res..

Hooper, A., Zebker, H., Segall, P., Kampes, B., 2004. A new method for measuring deformation on volcanoes and other natural terrains using InSAR persistent scatterers. Geophys. Res. Lett. 31, http://dx.doi.org/10.1029/2004GL021737.

Hrysiewicz, A., Wang, X., Holohan, E.P., 2023. EZ-InSAR: An easy-to-use open-source toolbox for mapping ground surface deformation using satellite interferometric synthetic aperture radar. Earth Sci. Inform. 16, 1929–1945. http://dx.doi.org/10.1007/s12145-023-00973-1.

Hyvärinen, A., Karhunen, J., Oja, E., 2001. Independent Component Analysis. Wiley, http://dx.doi.org/10.1002/0471221317.

Jasir, M.C.M., Sreejith, K.M., Agrawal, R., Begum, S.K., 2024. Application of singular spectrum analysis to InSAR time-series for constraining the post-seismic deformation due to moderate magnitude earthquakes: the case of 2019 M_w 6 Mirpur earthquake, NW Himalaya. Geophys. J. Int. 239, 637–645. http://dx.doi.org/10.1093/gji/ggae287.

Ketelaar, G., Bähr, H., Liu, S., Piening, H., van der Veen, W., Hanssen, R., van Leijen, F., van der Marel, H., Samiei-Esfahany, S., 2020. Integrated monitoring of subsidence due to hydrocarbon production: consolidating the foundation. Proc. Int. Assoc. Hydrol. Sci. 382, 117–123. http://dx.doi.org/10.5194/piahs-382-117-2020.

Lazecký, M., Spaans, K., González, P.J., Maghsoudi, Y., Morishita, Y., Albino, F., Elliott, J., Greenall, N., Hatton, E., Hooper, A., Juncu, D., McDougall, A., Walters, R.J., Watson, C.S., Weiss, J.R., Wright, T.J., 2020. LiCSAR: An automatic InSAR tool for measuring and monitoring tectonic and volcanic activity. Remote. Sens. 12, 2430. http://dx.doi.org/10.3390/rs12152430.

Lim, B., Zohren, S., 2021. Time-series forecasting with deep learning: a survey. Philos. Trans. R. Soc. A: Math. Phys. Eng. Sci. 379, 20200209. http://dx.doi.org/10.1098/rsta.2020.0209.

Liu, G., Ding, X., Li, Z., Li, Z., Chen, Y., Yu, S., 2004. Pre- and co-seismic ground deformations of the 1999 Chi-Chi, Taiwan earthquake, measured with SAR interferometry. Comput. Geosci. 30, 333–343. http://dx.doi.org/10.1016/j.cageo.2003.08.011.

Liu, J.-K., Lin, E.-K., Hsu, W.-C., Yu, F.-C., Chang, K.-T., Liou, Y.-A., 2014. Land subsidence monitoring with a network of continuously operating GPS stations in Yunlin County, middle Taiwan. In: 2014 IEEE Geoscience and Remote Sensing Symposium. IEEE, pp. 4247–4249. http://dx.doi.org/10.1109/IGARSS.2014.6947426.

Lomb, N.R., 1976. Least-squares frequency analysis of unequally spaced data. Astrophys. Space Sci. 39, 447–462. http://dx.doi.org/10.1007/BF00648343.

Mancini, F., Grassi, F., Cenni, N., 2021. A workflow based on SNAP–StaMPS open-source tools and GNSS data for PSI-based ground deformation using dual-orbit sentinel-1 data: Accuracy assessment with error propagation analysis. Remote. Sens. 13, 753. http://dx.doi.org/10.3390/rs13040753.

Marsaglia, G., Tsang, W.W., 1984. A fast, easily implemented method for sampling from decreasing or symmetric unimodal density functions. SIAM J. Sci. Stat. Comput. 5, 349–359. http://dx.doi.org/10.1137/0905026.

Massonnet, D., Feigl, K.L., 1998. Radar interferometry and its application to changes in the earth's surface. Rev. Geophys. 36, 441–500. http://dx.doi.org/10.1029/97RG03139.

Michelle, S., Ikehara, M., Galloway Devin, L., Falk, A., 2001. Detection and measurement of land subsidence using global positioning system and interferometric synthetic aperture radar, Coachella Valley, California, 1996-98. http://dx.doi.org/10.3133/wri014193.

Mirmazloumi, S.M., Wassie, Y., Navarro, J.A., Palamà, R., Krishnakumar, V., Barra, A., Cuevas-González, M., Crosetto, M., Monserrat, O., 2022. Classification of ground deformation using sentinel-1 persistent scatterer interferometry time series. GIScience Remote. Sens. 59, 374–392. http://dx.doi.org/10.1080/15481603.2022.2030535.

Moreira, A., Prats-Iraola, P., Younis, M., Krieger, G., Hajnsek, I., Papathanassiou, K.P., 2013. A tutorial on synthetic aperture radar. IEEE Geosci. Remote. Sens. Mag. 1, 6–43. http://dx.doi.org/10.1109/MGRS.2013.2248301.

Morishita, Y., Lazecky, M., Wright, T., Weiss, J., Elliott, J., Hooper, A., 2020. LiCSBAS: An open-source InSAR time series analysis package integrated with the LiCSAR automated sentinel-1 InSAR processor. Remote. Sens. 12, 424. http://dx.doi.org/10.3390/rs12030424.

Osmanoğlu, B., Sunar, F., Wdowinski, S., Cabral-Cano, E., 2016. Time series analysis of InSAR data: Methods and trends. ISPRS J. Photogramm. Remote Sens. 115, 90–102. http://dx.doi.org/10.1016/j.isprsjprs.2015.10.003.

Park, S.-W., Hong, S.-H., 2021. Nonlinear modeling of subsidence from a decade of InSAR time series. Geophys. Res. Lett. 48, http://dx.doi.org/10.1029/2020GL090970.

Pedretti, L., Bordoni, M., Vivaldi, V., Figini, S., Parnigoni, M., Grossi, A., Lanteri, L., Tararbra, M., Negro, N., Meisina, C., 2023. Interpolation of InSAR time series for the detection of ground deformation events (onthemove): application to slow-moving landslides. Landslides 20, 1797–1813. http://dx.doi.org/10.1007/s10346-023-02073-z.

Radman, A., Akhoondzadeh, M., Hosseiny, B., 2021. Integrating InSAR and deep-learning for modeling and predicting subsidence over the adjacent area of Lake Urmia, Iran. GIScience Remote. Sens. 58, 1413–1433. http://dx.doi.org/10.1080/15481603.2021.1991689.

Raspini, F., Caleca, F., Soldato, M.D., Festa, D., Confuorto, P., Bianchini, S., 2022. Review of satellite radar interferometry for subsidence analysis. Earth-Sci. Rev. 235, 104239. http://dx.doi.org/10.1016/j.earscirev.2022.104239.

Roque, D., Falcão, A.P., Perissin, D., Amado, C., Lemos, J.V., Fonseca, A., 2023. SARClust—A new tool to analyze InSAR displacement time series for structure monitoring. Sustainability 15, 3728. http://dx.doi.org/10.3390/su15043728.

Scargle, J.D., 1982. Studies in astronomical time series analysis. II - statistical aspects of spectral analysis of unevenly spaced data. Astrophys. J. 263, 835. http://dx.doi.org/10.1086/160554.

Shumway, R.H., Stoffer, D.S., 2011. Time Series Analysis and its Applications. Springer New York, New York, NY, http://dx.doi.org/10.1007/978-1-4419-7865-3.

Soldato, M.D., Solari, L., Raspini, F., Bianchini, S., Ciampalini, A., Montalti, R., Ferretti, A., Pellegrineschi, V., Casagli, N., 2019. Monitoring ground instabilities using SAR satellite data: A practical approach. ISPRS Int. J. Geo- Inf. 8, 307. http://dx.doi.org/10.3390/ijgi8070307.

Spaans, K., Hooper, A., 2016. InSAR processing for volcano monitoring and other near-real time applications. J. Geophys. Res.: Solid Earth 121, 2947–2960. http://dx.doi.org/10.1002/2015JB012752.

Springford, A., Eadie, G.M., Thomson, D.J., 2020. Improving the Lomb–scargle periodogram with the Thomson multitaper. Astron. J. 159, 205. http://dx.doi.org/10.3847/1538-3881/ab7fa1.

Su, Y., Peng, J., Shi, M., Guo, C., Ma, X., Li, X., Wang, J., Wang, W., 2024. An M-estimation method for InSAR nonlinear deformation modeling and inversion. IEEE Trans. Geosci. Remote Sens. 62, 1–12. http://dx.doi.org/10.1109/TGRS.2024.3362364.

Tesauro, M., Berardino, P., Lanari, R., Sansosti, E., Fornaro, G., Franceschetti, G., 2000. Urban subsidence inside the city of Napoli (Italy) observed by satellite radar interferometry. Geophys. Res. Lett. 27, 1961–1964. http://dx.doi.org/10.1029/2000GL008481.

Trenkler, G., 1995. Statistical distributions: M. Evans, N. Hastings and B. Peacock (1993): (2nd edition). New: John wiley. 170 pages, ISBN 0-471-55951,[pound sign] 24.95. Comput. Statist. Data Anal. 19, 483–484, URL: https://EconPapers.repec.org/RePEc:eee:csdana:v:19:y:1995:i:4:p:483-484.

VanderPlas, J.T., 2018. Understanding the lomb–scargle periodogram. Astrophys. J. Suppl. Ser. 236, 16. http://dx.doi.org/10.3847/1538-4365/aab766.

Vanicek, P., Castle, R.O., Balazs, E.I., 1980. Geodetic leveling and its applications. Rev. Geophys. 18, 505–524. http://dx.doi.org/10.1029/RG018i002p00505.

Vecchi, E., Tavasci, L., Giorgini, E., Gandolfi, S., 2024. A priori estimation of radar satellite interferometry's sensitivity for landslide monitoring in the Italian Emilia-Romagna region. Remote. Sens. 16, 2562. http://dx.doi.org/10.3390/rs16142562.

Vio, R., Diaz-Trigo, M., Andreani, P., 2013. Irregular time series in astronomy and the use of the lomb-scargle periodogram. Astron. Comput..

Wang, Z., Guo, L., Gong, H., Li, X., Zhu, L., Sun, Y., Chen, B., Zhu, X., 2023b. Land subsidence simulation based on extremely randomized trees combined with Monte Carlo algorithm. Comput. Geosci. 178, 105415. http://dx.doi.org/10.1016/j.cageo.2023.105415.

Wang, J., Li, C., Li, L., Huang, Z., Wang, C., Zhang, H., Zhang, Z., 2023a. InSAR time-series deformation forecasting surrounding salt lake using deep transformer models. Sci. Total Environ. 858, 159744. http://dx.doi.org/10.1016/j.scitotenv.2022.159744.

Wegmller, U., Strozzi, T., Wiesmann, A., 2001. GAMMA SAR and interferometric processing software. In: Proceedings of the ERS-Envisat Symposium.

Weiss, J.R., Walters, R.J., Morishita, Y., Wright, T.J., Lazecky, M., Wang, H., Hussain, E., Hooper, A.J., Elliott, J.R., Rollins, C., Yu, C., González, P.J., Spaans, K., Li, Z., Parsons, B., 2020. High-resolution surface velocities and strain for anatolia from sentinel-1 InSAR and GNSS data. Geophys. Res. Lett. 47, http://dx.doi.org/10.1029/2020GL087376.

Xiong, S., Wang, C., Qin, X., Zhang, B., Li, Q., 2021. Time-series analysis on persistent scatter-interferometric synthetic aperture radar (PS-InSAR) derived displacements of the hong Kong–Zhuhai–Macao bridge (HZMB) from sentinel-1A observations. Remote. Sens. 13, 546. http://dx.doi.org/10.3390/rs13040546.

Young, G., 1989. Geodetic Leveling. Kluwer Academic Publishers, Dordrecht, pp. 470–474. http://dx.doi.org/10.1007/0-387-30752-4_56.

Yu, C., Li, Z., Penna, N.T., 2018a. Interferometric synthetic aperture radar atmospheric correction using a GPS-based iterative tropospheric decomposition model. Remote Sens. Environ. 204, 109–121. http://dx.doi.org/10.1016/j.rse.2017.10.038.

Yu, C., Li, Z., Penna, N.T., Crippa, P., 2018b. Generic atmospheric correction model for interferometric synthetic aperture radar observations. J. Geophys. Res.: Solid Earth 123, 9202–9222. http://dx.doi.org/10.1029/2017JB015305.

Yu, B., Liu, G., Li, Z., Zhang, R., Jia, H., Wang, X., Cai, G., 2013. Subsidence detection by TerraSAR-X interferometry on a network of natural persistent scatterers and artificial corner reflectors. Comput. Geosci. 58, 126–136. http://dx.doi.org/10.1016/j.cageo.2013.04.020.

Yu, C., Penna, N.T., Li, Z., 2017. Generation of real-time mode high-resolution water vapor fields from GPS observations. J. Geophys. Res.: Atmos. 122, 2008–2025. http://dx.doi.org/10.1002/2016JD025753.

Zechmeister, M., Kürster, M., 2009. The generalised lomb-scargle periodogram. Astron. Astrophys. 496, 577–584. http://dx.doi.org/10.1051/0004-6361:200811296.

Zeiler, A., Faltermeier, R., Keck, I.R., Tome, A.M., Puntonet, C.G., Lang, E.W., 2010. Empirical mode decomposition - an introduction. In: The 2010 International Joint Conference on Neural Networks. IJCNN, IEEE, pp. 1–8. http://dx.doi.org/10.1109/IJCNN.2010.5596829.

Zuccarini, A., Giacomelli, S., Severi, P., Berti, M., 2024. Long-term spatiotemporal evolution of land subsidence in the urban area of Bologna, Italy. Bull. Eng. Geol. Environ. 83, 35. http://dx.doi.org/10.1007/s10064-023-03517-5.